ADVANCED FUNCTIONAL MATERIALS
www.afm-journal.de

Vapor–Liquid Transition-Based Broadband Light Modulation for Self-Adaptive Thermal Management

Chenglin Zhang, Jinlong Yang, Yong Li, Jianing Song, Junchang Guo, Yuanlai Fang, Xiao Yang, Qichang Yang, Dehui Wang, and Xu Deng**

Considerable research efforts have aimed to control indoor temperatures to improve daily life and industrial production. However, current strategies, which involve active regulation of energy input or passive regulation of sunlight transmission, cannot control indoor temperatures under all weather conditions. Herein, a self-adaptive thermal management device (STMD) that uses solar energy (heating) and radiative cooling (cooling) by exploiting the temperature differences across the device is reported. The adaptive heating and cooling functions are achieved by modulating sunlight transmittance and reflectance using a porous SiO_2 coating separated/merged with a refractive index-matched liquid which serves as a shutter. As a result, the STMD in the opaque mode exhibits low transmittance and in the transparent mode exhibits sufficiently high solar transmittance. Taking advantage of this self-regulated shuttering mechanism, the developed STMD enables i) an increase of ≈10 °C relative to the ambient temperature under a solar intensity of 400 W m^{-2} in cold weather and ii) a temperature reduction of ≈5 °C under a solar intensity exceeding 900 W m^{-2} in hot weather. The described design strategy offers an approach for constructing smart light-controlling devices and thermal-controlling building materials.

1. Introduction

Maintaining a desirable indoor temperature is crucial to agricultural, industrial production, and daily life.[1–3] Conventional thermal management devices, including air conditioners, electric fans, or floor heating systems, require external power input to regulate indoor temperatures. Such temperature-regulation devices account for >50% of the total energy consumption in residential buildings,[4] thereby conflicting with global goals related to carbon neutrality. Therefore, there is an urgent need to develop energy-efficient methods for temperature management with low-carbon emissions.

Solar irradiation (with a power of up to 1250 W m^{-2}) represents a clean energy source,[5] which already provides heat to objects on the earth. Controlling solar irradiance is important for maintaining indoor temperatures. In other words, the transmission of solar irradiation can be exploited to elevate indoor temperatures in cold weather.[6] Moreover, the reflection of solar irradiation can prevent indoor environments from undesired increases in temperature. To further decrease the temperature, it is possible to implement objects that can passively dissipate heat to outer space via the atmospheric long-wave infrared (LWIR) transparency window ($\lambda \approx$ 8–13 µm).[7–14] In general, all-day temperature management requires the self-adaptive modulation of radiation. Several techniques were recently introduced by switching the emissivity of electron materials or the transmission of passive cooling materials.[15–18] Although these strategies were successful in terms of switching material properties, they either neglected the modulation of the energy-dense solar spectrum or required an external stimulus to trigger the transmission transition.

In the present work, we developed a self-adaptive thermal management device (STMD) that modulates sunlight transmittance and reflection, thus enabling radiative cooling. The adaptability mechanism was elucidated on the basis of the vapor-to-liquid transition in the porous structures with temperature differences. A multi-layered structure was observed in the porous coating, exhibiting only 11% transmittance in the opaque mode. When a refractive index-matched liquid replaced the air in these structures, the solar transmittance reached 94% in the transparent mode, resulting in a high solar modulation (83%). The complete switching process was achieved within 3 min, and stable performance was observed even after 500 switching iterations. The temperature increased by ≈10 °C in cold weather and decreased by ≈5 °C in hot weather, which saved 55 and

C. Zhang, J. Yang, J. Song, J. Guo, Y. Fang, D. Wang, X. Deng
Institute of Fundamental and Frontier Sciences
University of Electronic Science and Technology of China
Chengdu 610054, P. R. China
E-mail: wangdehui@uestc.edu.cn; dengxu@uestc.edu.cn
Y. Li
Digital Media Art Key Laboratory of Sichuan Province
Sichuan Conservatory of Music
Chengdu 610021, P. R. China
X. Yang, Q. Yang
Institute of Urban Agriculture
Chinese Academy of Agricultural Sciences
Chengdu 610218, P. R. China
X. Deng
Shenzhen Institute for Advanced Study
University of Electronic Science and Technology of China
Shenzhen 518110, P. R. China
The ORCID identification number(s) for the author(s) of this article can be found under https://doi.org/10.1002/adfm.202208144.

DOI: 10.1002/adfm.202208144

51 MJ m^{-2} of energy, respectively. The self-adaptive indoor thermal manipulation achieved by this smart device has diverse applicability in commercial buildings, residential households, and glass greenhouses.

2. Results and Discussion

2.1. Design Principles

To endow the STMD with multiple desired characteristics (i.e., high solar modulation ability, self-regulation, and no external energy input), we applied a facile method whereby nano/micro-particles were used to form a porous coating with a switchable operating state; the coating was wither immersed in a specific liquid or used alone. The heating and cooling functions originated from a response to the temperature difference across the device, according to the refractive index-matched liquid wetting/de-wetting of the porous SiO_2 coating. The working principle is shown in **Figure 1**a. In hot weather, the outdoor temperature (T_o) is generally higher than the indoor temperature (T_i), whereas the situation is reversed in cold weather.

The temperature difference could be readily used to control the phase change of liquid–vapor–liquid on the walls if the device was sealed inside a closed chamber with high vapor saturation (Figure 1a, inset). For example, in summer, the high outdoor temperature causes the liquid to detach from the porous coating through volatilization (Figure 1a, inset left). The dry porous SiO_2 coating reflects most of the sunlight, thus cooling the indoor space as a radiative cooling material. In this opaque mode, the device has low transmittance in the solar wavelength range, thereby reducing the temperature. In winter, the liquid evaporates from the non-coating side, condenses on the coating surface, and then penetrates the porous structures (Figure 1a, inset right). Upon wetting, the transmittance increased dramatically, and the device became highly transparent. Thus, solar irradiation could transmit through the device and increase the indoor temperature through solar heating.

The mechanisms governing sunlight reflection and transmission are illustrated in Figure 1b, which shows that the scattering behavior is tuned on the basis of the refractive index differences between the coating/air and coating/liquid. The STMD preparation process is shown in Figure S1 (Supporting Information). First, uniformly-sized SiO_2 particles were dispersed in ethanol by an ultrasonic treatment. The evenly distribute mixture was then cast on a clean glass substrate. During the evaporation of ethanol, the movement of particles is dominated by the capillary force. The gradual decrease in the meniscus between SiO_2 particles drags them to assemble tightly into a densely-packed porous structure and form a superhydrophilic

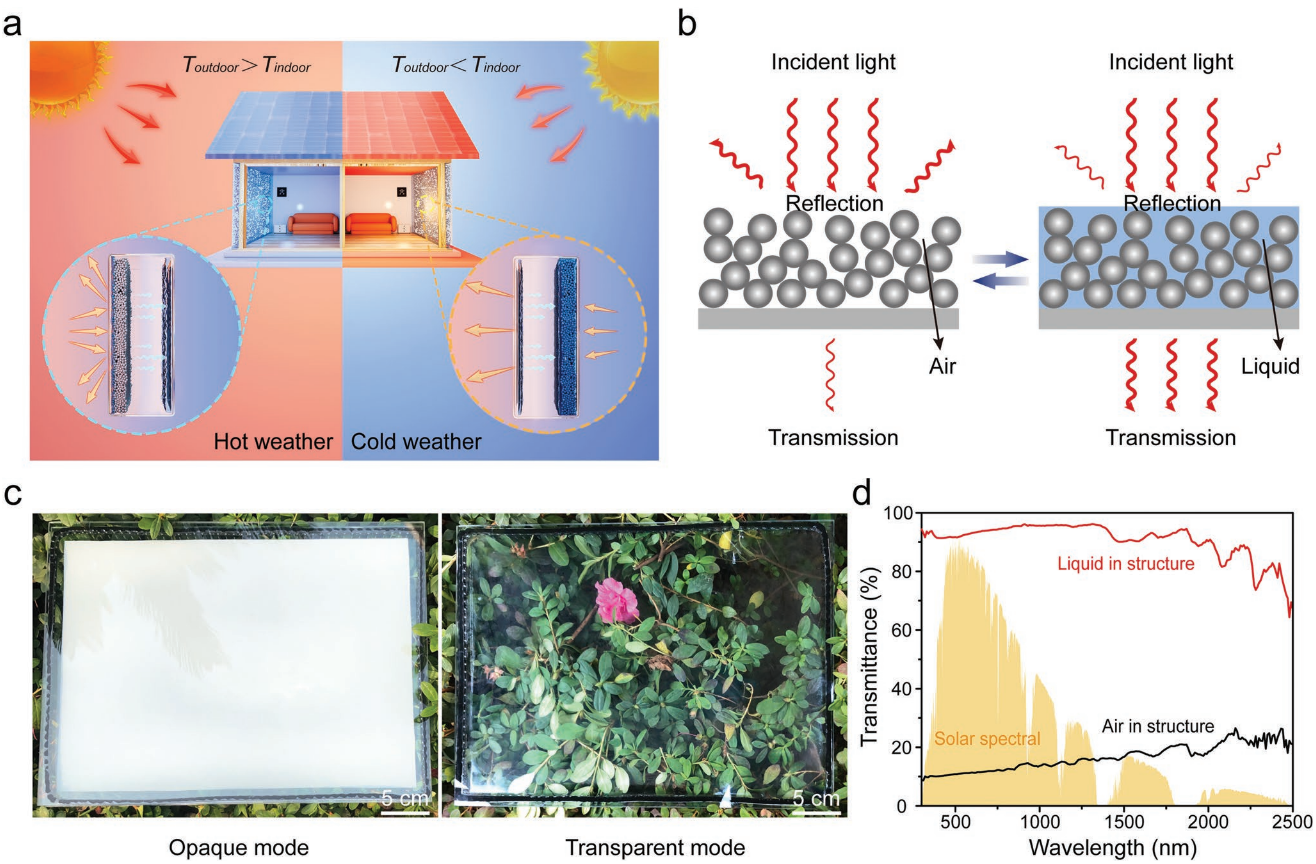

Figure 1. Design of the self-adaptive thermal management device (STMD). a) Working principle of the STMD in hot and cold weather; b) mechanism of light transmission and reflection; c) optical photographs of a 400 mm × 300 mm × 10 mm STMD in transparent and opaque mode; d) transmittance performance of the STMD at different working states.

coating (Figure S2, Supporting Information). Then, carbon tetrachloride was dropped onto the coating and spread rapidly over the surface. The obtained coating/liquid composite was immediately sealed in a closed chamber to assemble the final STMD. Figure 1c shows the two states of a large-scale (400 mm × 300 mm × 10 mm) fabricated STMD. The device was opaque under the coating/liquid-separated state, and the plant was invisible (Figure 1c, left). Spectral reflectance results indicated that ultraviolet, visible, and near-infrared wavelengths were rarely transmitted when the air filled in the structure (Figure 1d). In contrast, after the liquid merged with the coating, the device became transparent, thus revealing the plant with a red flower (Figure 1c, right). In this case, the solar transmittance (τ_{sol}) increased from 0.13 to 0.93, yielding a solar modulation ability ($\Delta\tau$ = 0.93–0.13 = 0.80) in Figure 1d. This dramatic transition is expected to allow for control across most of the solar irradiance spectrum.

2.2. Solar Radiation Regulation

To achieve highly efficient solar radiation modulation, we explored various coating materials, liquids, and fabrication methods. First, SiO_2 particles were selected as the optimal materials for the porous coating because they do not absorb sunlight,[19] have a low refractive index (beneficial for finding a matching liquid), and exhibit high mid-infrared emissivity (Figure S3a,b, Supporting Information). Second, the liquid used in the STMD should follow the refractive index matching mechanism. When the porous coating is in a dry state, the large refractive index difference ($\Delta n = n_{silica} - n_{air} = 1.458 - 1 = 0.458$) between the particles and the air causes an efficient scattering of solar wavelengths.[20–22] However, when the coating is wetted using a refractive index-matched liquid (e.g., carbon tetrachloride; $n_{CCl4} \approx 1.454$), Δn decreased dramatically to 0.004 (i.e., $\Delta n = n_{silica} - n_{CCl4}$). This reduces the scattering efficiency of the particles by more than one order of magnitude, and the coating becomes transparent (Figure 1c). Figure S4 (Supporting Information) shows the effect of n-matching on the optical transparency of the porous SiO_2 coating when using various liquids, including water (n_{water} = 1.332), acetic acid ($n_{acetic\ acid}$ = 1.358), glycol (n_{glycol} = 1.431), glycerol ($n_{glycerol}$ = 1.466), and cedar oil ($n_{cedar\ oil}$ = 1.515). The corresponding optical images are shown in Figure S5 (Supporting Information).

We then investigated the influence of the porous coating structure on the optical modulation performance of the STMD. For a single-layered porous coating (**Figure 2**a), the transmittance of sunlight at the coating/liquid-separated state decreases as the particle size increases (Figure S6, Supporting Information). The black curves in Figure S6 (Supporting Information) demonstrate that nanoscale spheres scatter light with short wavelengths but transmit light with long wavelengths. As the particle size increases, microscale spheres enable the scattering of light with long wavelengths and the transmittance of light with short wavelengths. Because of the similar transmittance at the coating/liquid merged state, $\Delta\tau$ increased gradually to 0.70 as the particle diameter increased from 100 nm to 5 µm at a constant thickness (Figure 2b). The corresponding optical images are shown in Figure S7 (Supporting Information). This phenomenon can be explained by the Mie scattering theory,[22] which predicts efficient scattering across the broadband spectrum of sunlight by integrating SiO_2 particles at distinct diameters. Simply, efficient scattering occurs when particle size (d) is approximately comparable to the incident light wavelength (λ).[21] The peak scattering efficiency (Q_s) is determined on the basis of the size of SiO_2 particles at various solar wavelengths, and this parameter was computed using finite-difference-time-domain (FDTD) simulations (Figure S8, Supporting Information). The results in Figure 2c show that the scattering efficiency of microscale spheres was much higher than that of nanoscale spheres, and the peak of scattering efficiency red-shifted as the particle size increased. Spheres with diameters of 500 nm, 1 µm, 2 µm, and 3 µm had resonance wavelengths at 400, 750, 1300, and 2100 nm, respectively. Notably, SiO_2 particles had low Q_s when their diameters were below 500 nm, and there was no evident Q_s peak in the solar spectrum when the particle diameter exceeded 5 µm. In this work, we chose particles with diameters in the range of 0.5–5 µm to fabricate multi-layered porous coatings with maximized scattering efficiency. The images in Figure 2d–f show coatings with the same thickness (≈60 µm) comprising two, three, or four layers made from closely-packed SiO_2 particles. From the bottom to the top layer, the four-layered coating was packed with SiO_2 particles having diameters of 500 nm, 1 µm, 2 µm, and 3 µm, respectively. Various combinations were tested to optimize $\Delta\tau$, and it was determined that the four-layered coating enabled the best modulation ability ($\Delta\tau$ = 0.83), as shown in Figure 2g. We also tried the five-layered porous coating at the same thickness by adding a layer of SiO_2 particles with a diameter of 5 µm. The results are demonstrated in Figure S9a (Supporting Information), indicating no improvement in the reflectance of sunlight by increasing the layer. Similarly, the coating made by mixed SiO_2 particles of 500 nm, 1 µm, 2 µm, and 3 µm demonstrates an inferior transmission performance compared with the layer-by-layer fabricated coating (Figure S9b, Supporting Information) in the opaque mode. Nevertheless, the transparent mode of both coatings is almost identical. Meanwhile, the absorbance efficiency Q_a of SiO_2 particles was similar regardless of whether the device was under a separated or merged state (Figure 2h). This result indicates that the transmittance is tuned by scattering, according to the difference in the refractive index, rather than by the absorbance. Figure S10 (Supporting Information) shows that the Q_s of SiO_2 particles decrease appreciably throughout the solar wavelength range after wetting with carbon tetrachloride; thus, it was concluded that light exhibits ballistic transmittance in the coating/liquid merged state. The transmittance spectra of STMD with different coating thicknesses are shown in Figure 2i. The inner porous coating comprised three-layer of SiO_2 particles with diameters of 500 nm, 1 µm, and 2 µm. The transmittance of the opaque state (τ_{opaque}) of the device decreased from 0.58 to 0.12 as the thickness increased from 20 to 140 µm, and this parameter decreased gradually after the thickness surpassed 120 µm. The variations in τ_{opaque} can be explained by the Beer–Lambert law.[23] The porous coating contains particle powders, which serve as scattering media. Under these conditions, the total transmittance τ passing through the coating with thickness l can be expressed as $\tau \sim l_t / l$,[24] where l_t is the transport mean free path. Thus, the τ is inversely

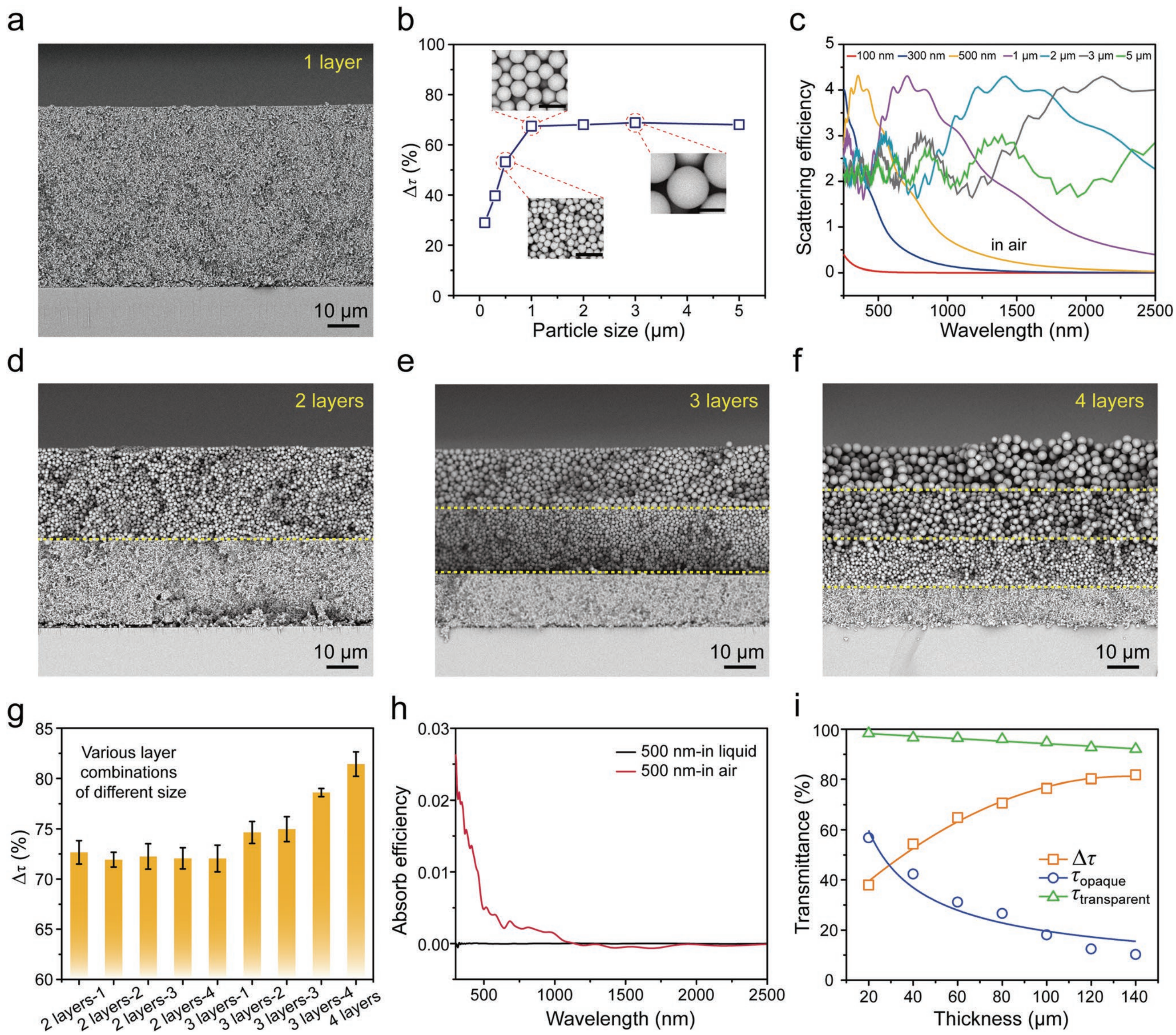

Figure 2. Morphology of the SiO_2 coating and underlying mechanism of light modulation. a) Scanning electron microscopy (SEM) images of single-layered coating (side view); b) transmittance difference as a function of particle size with SEM images of densely-packed particles (top view, scale bar = 2 μm); (c) scattering efficiency spectra of SiO_2 particles of various sizes as a function of solar wavelength in the air; d–f) SEM images of two-, three-, and four-layered coatings (side view); g) solar modulation by multi-layered SiO_2 coatings (composition details in Experimental section); h) absorbance efficiency of 500 nm SiO_2 particles in liquid and air; i) transmittance of the coating as a function of coating thickness.

proportional to l. Moreover, the transmittance of the transparent state ($\tau_{transparent}$) remains relatively high and slowly changes from 0.97 to 0.93, causing $\Delta\tau$ ($\tau_{transparent}$ - τ_{opaque}) to reach a maximum value of 0.80 at a thickness of 140 μm.

2.3. Self-Adaptive Switch Property

For functional STMD, the liquid requires a matched n as well as a low boiling point to tailor its state according to the environment. Carbon tetrachloride was selected because of its lower boiling point (78.3 °C) relative to other n-matched liquids (Figure S11, Supporting Information). We first show a full switching cycle where the temperature difference across the STMD was 15 °C (**Figure 3**a,b). The UESTC logo was placed underneath the STMD to indicate the state of the device. To capture the phase-change process of carbon tetrachloride from the SiO_2 coating to the glass slide, we set a camera close to the non-coated side, as shown in Figure 3a, left. Carbon tetrachloride was integrated within the porous structure initially, and the corresponding optical image at t = 0 s shows that the STMD was transparent (the logo can be seen clearly). When the coating side is at a higher temperature, carbon tetrachloride evaporates from the porous structure and condenses on the glass slide, thus forming a liquid film. The logo eventually became invisible at t = 133 s. In contrast, the phase-change

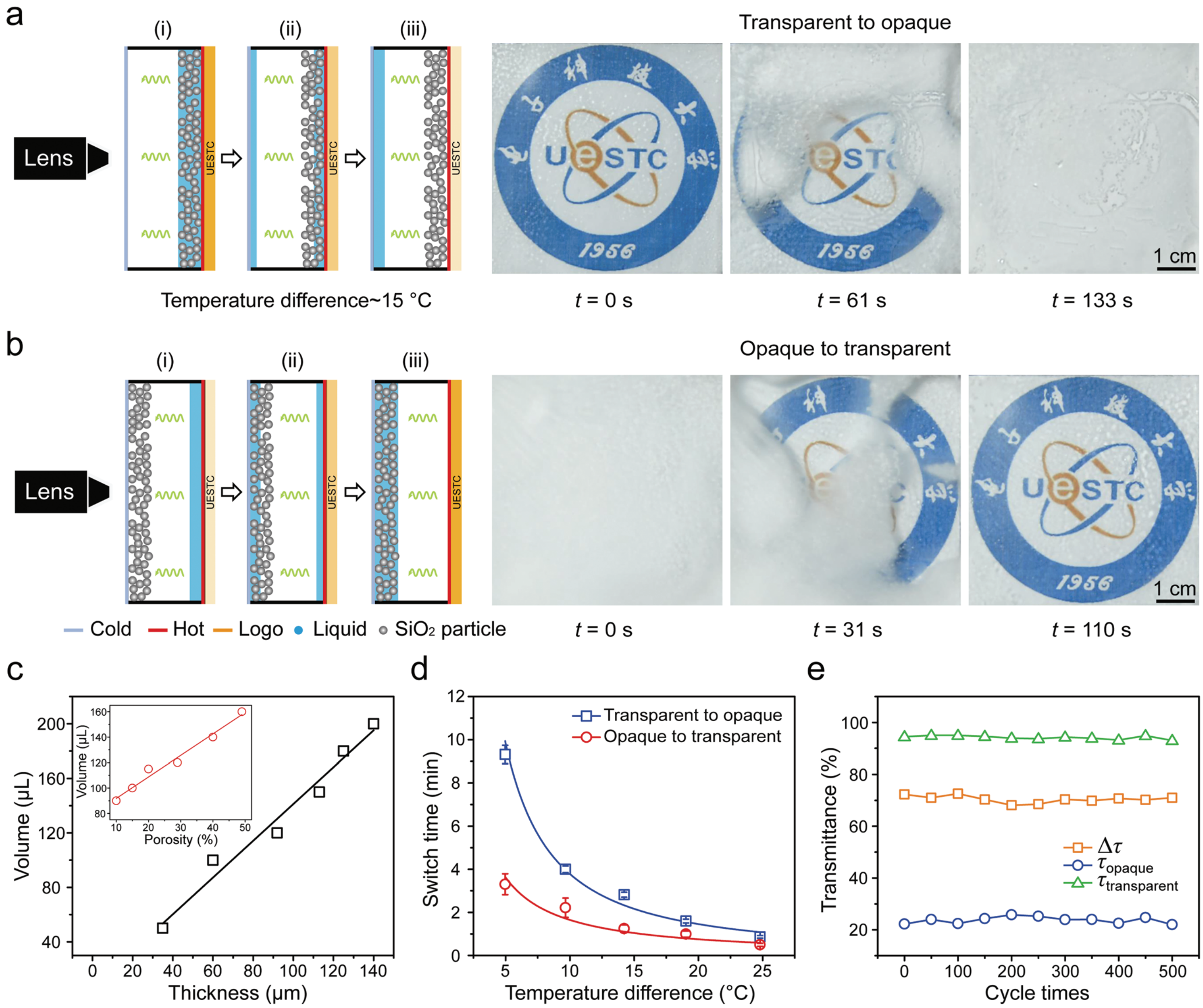

Figure 3. The switching process of an STMD under temperature difference≈15 °C. a,b) Schematic diagrams of the STMD observation system and time-lapse optical images of STMD switching; c) liquid volume as a function of coating thickness (inset: liquid volume as a function of porosity); d) switching time as a function of the temperature difference across the device; e) transmittance of STMD over 500 opaque-transparent cycles.

process of carbon tetrachloride from the glass slide to the SiO_2 coating was observed by setting the camera close to the coated side (Figure 3b, left). The STMD can change from opaque to transparent when the temperature on the glass side is higher, because carbon tetrachloride evaporates from the glass slide and condenses into the porous structures. The images in Figure 3b show the logo changing from invisible to clear following the liquid-vapor-liquid transition. The corresponding switching process is shown in Movie S1 (Supporting Information). It should be noted that the STMD functions in a proper carbon tetrachloride volume range. As shown in Figure 3c, the liquid volume is proportional to the coating thickness and porosity. As the coating thickness and porosity increase, more liquid is needed to fill the voids of the porous structures. For the device size used in this demonstration (a round STMD with a diameter of 5 cm), carbon tetrachloride with a volume of <60 µL only partially wets the porous coating, resulting in a partially transparent STMD. However, when the volume of carbon tetrachloride was ≥80 µL, it forms a thicker liquid film on the glass substrate, and the excess liquid returns to the porous coating due to gravity, resulting in a partially opaque state (Figure S12, Supporting Information).

To test the switching speed of the STMD at various temperature differences, we placed the STMD in a foam box to reduce the heat exchange. A schematic drawing of the test setup is shown in Figure S13 (Supporting Information). Two stages with a water cycling system were placed on the cell to create a temperature difference. Two thermocouples were placed in the cell to monitor the temperature change, and a glass cover was placed on the foam box to allow for observations of the STMD state. The results shown in Figure 3d reveal that the switching process from the opaque to transparent state is faster than the transparent-to-opaque switch for all temperature differences. This phenomenon can be attributed to two factors: i) a smaller liquid/air interface impedes liquid evaporation from the porous structures relative to a flat substrate, resulting in a slower transparent-to-opaque process; ii) a shorter vapor-to-liquid condensation process occurs on the superhydrophilic porous coating relative to the flat glass substrate because of the greater number of nucleation sites on the superhydrophilic porous coating, and this facilitates a more rapid opaque-to-transparent process. The total switching time decreased as the temperature difference increased. When the temperature difference reached 25 °C, the total switching time was within 3 min, which was comparable to some thermochromic, electrochromic, and photochromic systems.[25] The stability of the STMD was evaluated after 500 cycles between the transparent and opaque states (Figure 3e). The liquid could repeatedly evaporate and condense in the STMD with negligible mass loss. Therefore, $\tau_{transparent}$, τ_{opaque}, and $\Delta\tau$ decreased slightly to 0.15, 0.02, and 0.13, respectively. These results indicate that exploiting the phase change of the liquid has a limited effect on the porous coating prepared by drop-casting. Furthermore, an outdoor switching test was performed to demonstrate the practicality of STMD (Movie S2, Supporting Information). We used a custom-made polymethyl methacrylate (PMMA) box containing a potted plant and a water-circulating stage to simulate an indoor environment. In the morning, the outside temperature was lower than the inside temperature (Figure S14a, Supporting Information), and the STMD changed from opaque to transparent, which allowed sunlight to pass through the material to heat the inside. As the outside temperature gradually increased as noon approached (Figure S14b, Supporting Information), the STMD automatically transitioned to an opaque state.

2.4. Thermal Management Tests

As a proof-of-concept of the heating and cooling functions, we first tested the device as the temperature increased under a simulated solar source (equal to 1 sun) for 10 min. A black polyvinyl chloride (PVC) logo of "UESTC" stuck to the back of the STMD was observed to evaluate the state of the device (Figure S15, Supporting Information). In the opaque mode, the thermal images show that the temperature of the pattern increased slightly to 28.7 °C. In contrast, the temperature increased to 43.4 and 46.4 °C in the transparent mode and using bare glass, respectively, indicating the device's high thermal management abilities.

The cooling and heating properties of the STMD were verified on the basis of an outdoor test. As shown in **Figure 4**a, the testing apparatus comprised a polystyrene (PS) foam box wrapped with aluminum foil to block radiation from the surroundings. A thermocouple was placed in the box and connected to the bottom surface of the STMD to precisely monitor changes in temperature. Then, the STMD was installed on the foam, and a polyethylene (PE) film was used to seal the hole as a convection shield. The measurement apparatus was mounted on a 1-meter-high desk with an insulation board.

The entire measurement setup was placed on a roof in Chengdu, China under clear sky conditions, as shown in Figure S16 (Supporting Information). In hot weather, the device was continuously tested from 10:00 to 14:00 under a relative humidity of ≈32% and a wind speed of ≈1.5 m s^{-1} (Figure S17a, Supporting Information). Under these conditions, the STMD exhibited excellent light blocking abilities and a reflectance >94.1% in the solar radiation region (Figure S18a, Supporting

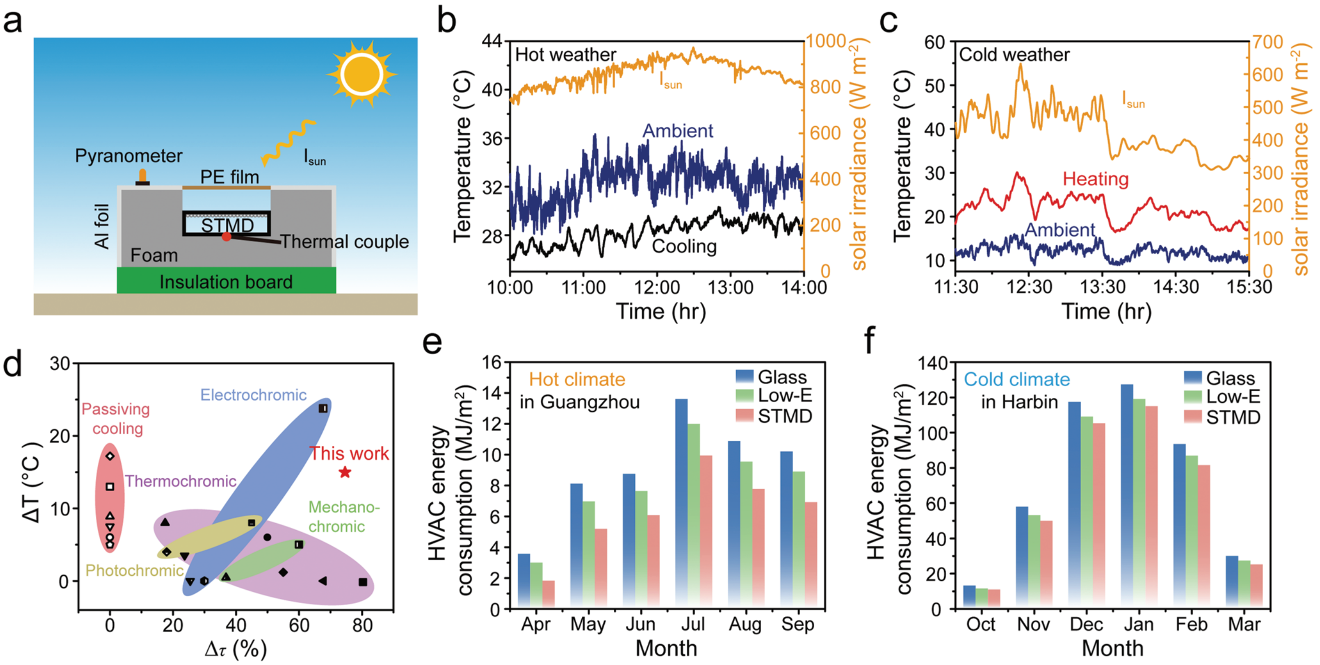

Figure 4. Practical applications of the developed STMD. a) Schematic diagram of the temperature change test apparatus; b,c) cooling and heating performances of the STMD under average solar irradiance of 850 and 400 W m^{-2}, respectively; d) comparison of temperature and sunlight modulation abilities of various reported methods.[11,12,26–39] e,f) simulations of HVAC energy consumption in Guangzhou and Harbin for normal glass, low-E glass, and the developed STMD.

Information). The corresponding $\Delta\tau$ was ≈0.72. The infrared emissivity spectrum (Figure S3b, Supporting Information) shows that the silica had a high average emissivity of 93.6% from 7 to 14 µm. The relatively high emissivity of this porous structure relative to solid SiO_2 films was attributed to the introduction of air, which improves optical impedance. The porous coating has an extinction peak at 9.7 µm corresponding to the LWIR window, which may be attributed to the phonon-enhanced Fröhlich resonances of the microspheres (Figure S18b, Supporting Information). As a result, it radiates heat in the LWIR window and is eventually emissive to outer space. As shown in Figure 4b, the STMD achieved a sub-ambient cooling of 5 °C under an average solar irradiance of 850 W m^{-2}, corresponding to a theoretical net cooling power of 85.1 W m^{-2} (Figure S19, Supporting Information). Owing to its high porosity (28%), the coating had a low thermal conductivity of 0.31 W m^{-1} K^{-1}, which can suppress heat exchange with the ambient atmosphere (Figure S20, Supporting Information).[40]

In cold weather, the STMD exhibited high solar transmittance after switching to the transparent mode, which allowed sunlight to transmit through the device to increase the indoor temperature via solar heating. The heating performance was tested continuously from 11:30 to 15:30 under a relative humidity of ≈72% and a wind speed of ≈0.8 m s^{-1} (Figure S17b, Supporting Information). As shown in Figure 4c, the temperature of the PVC film increased by 10°C compared with the ambient temperature (12 °C) under an average solar irradiance of 400 W m^{-2}. Therefore, the STMD demonstrated dynamic regulation of sunlight transmittance or reflectance to enable cooling or heating functionalities in varying diurnal or seasonal environments.

We benchmarked the temperature modulation (ΔT) and solar management abilities against reported methods for thermal management (Figure 4d). The reported radiative cooling materials in the pink circle show mono-functionality (i.e., cooling) and are unable to modulate solar irradiance. However, some electrochromic, mechanochromic, and thermochromic materials exhibit solar modulation abilities but lack temperature management. The materials that can exhibit these two functions simultaneously are inferior to the device developed herein, and the distinction is attributed to the discoloration mechanism.

To demonstrate the energy-saving effect of STMD, we simulated the monthly HVAC energy consumption in two typical cities: Guangzhou (hot weather) and Harbin (cold weather) (Figure S21 and Table S1, Supporting Information). As shown in Figure 4e, the developed device consumed ≈38 MJ m^{-2} energy to cool indoor temperatures in Guangzhou from April to September; this was less than normal glass (≈55 MJ m^{-2}) and low-E glass (≈48 MJ m^{-2}). In addition, when heating from October to March in Harbin, the STMD saved ≈51 and ≈19 MJ m^{-2} energy consumption compared with normal glass and low-E glass, respectively (Figure 4f).

3. Conclusion

In summary, we prepared a self-adaptive thermal management device to effectively control solar radiation using a porous coating reversibly wetted by a liquid. The underlying mechanism was elucidated through experiments and optical simulations, revealing that the modulation ability of the device can be tuned on the basis of the size of SiO_2 particles, the thickness of the porous coating, and the refractive index difference between the liquid and the particles. Compared with conventional strategies, such as thermochromic, electrochromic, photochromic, and mechanochromic systems, the method described herein demonstrates adaptive properties, high modulation abilities, a fast switching speed, and the integration of heating and cooling functionalities in a single device, thus highlighting its versatility in hot or cold weather. Therefore, this multifunctional device can serve as an alternative for eco-friendly and sustainable building components, including smart windows that can control indoor temperatures, as well as other applications.

4. Experimental Section

Materials: Monodisperse silica particles (SiO_2) with distinct sizes (100 nm, 300 nm, 500 nm, 1 µm, 2 µm, 3 µm, and 5 µm) were purchased from NanoMicro Technology Ltd. (Suzhou, China). Ethylene glycol, ethanol, acetic acid, glycerol, carbon tetrachloride, and cedar oil were purchased from Sigma–Aldrich. Glass slides (70 mm × 70 mm × 3 mm, 200 mm × 150 mm × 3 mm, and 400 mm × 300 mm × 10 mm) were purchased from Alibaba. The spacers with corresponding sizes, including Polytetrafluoroethylene (PTFE), Butyl, and aluminum (Al) were purchased from Alibaba, and the sealant (Agilent, Torr Seal AB glue) was also obtained from Alibaba.

Preparation of Self-Adaptive Thermal Management Devices: Glass slides were first thoroughly cleaned with 98% ethanol under ultrasonication and dried under nitrogen flow. Then, 2 g of monodisperse SiO_2 particles (500 nm, 1 µm, 2 µm, or 3 µm) were ultrasonically dispersed into 20 mL ethanol for 20 min. The clean substrate was placed horizontally on an optical platform. A blue film of the same size as the spacer was adhered to the glass slide to leave a margin for the substrate. Next, 1 mL of a suspended solution of 500-nm SiO_2 spheres was then drop-cast on a 70 mm × 70 mm × 3 mm glass slide. The glass slide was transferred to a hot stage (60 °C) for 5 min, and a single-layer porous coating was formed on the glass when the ethanol evaporated. Similarly, drop-casting suspended solutions of 1-, 2-, and 3-µm SiO_2 particles yielded the corresponding single-layer porous coatings. To fabricate two-layered porous coatings, second suspended solution of 1-, 2-, or 3-µm SiO_2 particles (1 mL) was drop-cast onto the first porous coating until the solvent evaporated completely. The three- and four-layered porous coatings were fabricated by dropping additional suspended solutions in the same manner as in the two-layered coatings. The coating thickness and large-scale coatings were controlled the solution volume. The fabricated multi-layered coatings in Figure 2g were: 2 layers-1 = 500 nm + 1 µm coating; 2 layers-2 = 500 nm + 2 µm coating; 2 layers-2 = 500 nm + 3 µm coating; 2 layers-4 = 1 µm + 2 µm coating; 3 layers-1 = 500 nm + 1 µm + 2 µm coating; 3 layers-2 = 500 nm + 1 µm + 3 µm coating; 3 layers-3 = 500 nm + 2 µm + 3 µm coating; 3 layers-4 = 1 µm + 2 µm + 3 µm coating; 4 layers = 500 nm + 1 µm + 2 µm + 3 µm coating. The spacer and the upper glass slide were then placed on the coated glass after removing the blue film. In our experiments, three different kinds of spacers were employed with distinct sealing processes. The butyl seal strip was adopted in Figure 1c which is able to seal by pressing. Polytetrafluoroethylene (PTFE) spacers were used and sealed by mechanical pressure which is convenient for characterization. The size of the spacer is 60 mm × 60 mm with a 5 mm margin in Figures S5 and S7 (Supporting Information), another spacer in Figure S12 (Supporting Information) is 50 mm in diameter, all the thickness of PTFE spacers is 3 mm. The Al spacer is 20 cm × 15 cm with a 1 cm margin, and 3 mm thick (Movie S1, Supporting Information). Then the edge of the device was sealed using the sealant and placed for 12 h at room temperature. Finally, the liquid was added to the chamber through a reserved hole.

Characterization: The morphology and thickness of the SiO_2 coatings were characterized using a scanning electron microscope (Phenom ProX, Netherlands) operating at 15 kV. The solar wavelength transmittance (from 300 to 2500 nm) of the SiO_2 coatings was characterized using a UV–Vis–NIR spectrophotometer (Perkin Elmer, Lambda 950) equipped with pre-calibrated and automatically-switched iodine tungsten and protium lamps. The reflectivity from 7–14 µm was measured using a Fourier transform infrared (FTIR) spectrophotometer equipped with a diffuse gold integrating sphere (Bruker Tensor 27, Germany). The refractive index and extinction coefficients in the wavelength range of 0.2–17 µm at 60° were measured for a pristine quartz substrate using an ellipsometer (V-VASE and IR-VASE, J. A. Woollam, USA). The thermal conductivities of distinct layered coatings were measured via a hot disk (Hot Disk TPS 2500s, Sweden).

Supporting Information

Supporting Information is available from the Wiley Online Library or from the author.

Acknowledgements

The authors acknowledge funding support by the National Natural Science Foundation of China (22072014), the Fundamental Research Funds for the Central Universities (ZYGX2019J119), the Chengdu Science and Technology Bureau (2021-GH02-00105-HZ), the Shenzhen Science and Technology Program (JCYJ20210324142210027), the Central Government Funds of Guiding Local Scientific and Technological Development for Sichuan Province (No. 2021ZYD0046), the Sichuan Outstanding Young Scholars Foundation (2021JDJQ0013), the Sichuan Science and Technology Program (2021JDRC0016), and the Major Project of Digital Media Art Key Laboratory of Sichuan Province (No.21DMAKL03). The authors thank Hongmei Zhong from CityU for FDTD simulations, Jihua Zou from UESTC for UV–VIS–IR spectrum characterization.

Conflict of Interest

The authors declare no conflict of interest.

Authors Contribution

C. Z. and D. W. conceived the project and designed the experiments. X. D. supervised the research. C. Z. carried out the experiment. C. Z., J. Y., D. W., and X. D. analyzed the data and wrote the paper. All authors contributed to paper revision and have given approval to the final version of the manuscript.

Data Availability Statement

The data that support the findings of this study are available in the supplementary material of this article.

Keywords

heat management, light management, phase transition, radiative cooling, self-adaptive thermal management, wettability

Received: July 16, 2022
Revised: August 25, 2022
Published online:

[1] X. Li, B. Sun, C. Sui, A. Nandi, H. Fang, Y. Peng, G. Tan, P.-C. Hsu, *Nat. Commun.* **2020**, *11*, 6101.
[2] X. A. Zhang, S. Yu, B. Xu, M. Li, Z. Peng, Y. Wang, S. Deng, X. Wu, Z. Wu, M. Ouyang, Y. Wang, *Science* **2019**, *363*, 619.
[3] C. Zhao, B. Liu, S. Piao, X. Wang, B. Lobell David, Y. Huang, M. Huang, Y. Yao, S. Bassu, P. Ciais, J.-L. Durand, J. Elliott, F. Ewert, A. Janssens Ivan, T. Li, E. Lin, Q. Liu, P. Martre, C. Müller, S. Peng, J. Peñuelas, C. Ruane Alex, D. Wallach, T. Wang, D. Wu, Z. Liu, Y. Zhu, Z. Zhu, S. Asseng, *Proc. Natl. Acad. Sci. USA* **2017**, *114*, 9326.
[4] Y. Ke, C. Zhou, Y. Zhou, S. Wang, S. H. Chan, Y. Long, *Adv. Funct. Mater.* **2018**, *28*, 1800113.
[5] J. Wang, J. Sun, T. Guo, H. Zhang, M. Xie, J. Yang, X. Jiang, Z. Chu, D. Liu, S. Bai, *Adv. Mater. Technol.* **2022**, *7*, 2100528.
[6] D. Zhao, J. Ji, H. Yu, X. Zhao, *Energy and Build* **2019**, *182*, 242.
[7] A. P. Raman, M. A. Anoma, L. Zhu, E. Rephaeli, S. Fan, *Nature* **2014**, *515*, 540.
[8] S. Zeng, S. Pian, M. Su, Z. Wang, M. Wu, X. Liu, M. Chen, Y. Xiang, J. Wu, M. Zhang, Q. Cen, Y. Tang, X. Zhou, Z. Huang, R. Wang, A. Tunuhe, X. Sun, Z. Xia, M. Tian, M. Chen, X. Ma, L. Yang, J. Zhou, H. Zhou, Q. Yang, X. Li, Y. Ma, G. Tao, *Science* **2021**, *373*, 692.
[9] T. Li, Y. Zhai, S. He, W. Gan, Z. Wei, M. Heidarinejad, D. Dalgo, R. Mi, X. Zhao, J. Song, J. Dai, C. Chen, A. Aili, A. Vellore, A. Martini, R. Yang, J. Srebric, X. Yin, L. Hu, *Science* **2019**, *364*, 760.
[10] D. Li, X. Liu, W. Li, Z. Lin, B. Zhu, Z. Li, J. Li, B. Li, S. Fan, J. Xie, J. Zhu, *Nat. Nanotechnol.* **2021**, *16*, 153.
[11] T. Wang, Y. Wu, L. Shi, X. Hu, M. Chen, L. Wu, *Nat. Commun.* **2021**, *12*, 365.
[12] A. Leroy, B. Bhatia, C. C. Kelsall, A. Castillejo-Cuberos, M. H. Di Capua, L. Zhao, L. Zhang, A. M. Guzman, E. N. Wang, *Sci. Adv.* **2019**, *5*, eaat9480.
[13] Y. Zhai, Y. Ma, S. N. David, D. Zhao, R. Lou, G. Tan, R. Yang, X. Yin, *Science* **2017**, *355*, 1062.
[14] N. Shi Norman, C.-C. Tsai, F. Camino, D. B. Gary, N. Yu, R. Wehner, *Science* **2015**, *349*, 298.
[15] S. Wang, T. Jiang, Y. Meng, R. Yang, G. Tan, Y. Long, *Science* **2021**, *374*, 1501.
[16] K. Tang, K. Dong, J. Li, P. Gordon Madeleine, G. Reichertz Finnegan, H. Kim, Y. Rho, Q. Wang, C.-Y. Lin, P. Grigoropoulos Costas, A. Javey, J. Urban Jeffrey, J. Yao, R. Levinson, J. Wu, *Science* **2021**, *374*, 1504.
[17] H. Zhao, Q. Sun, J. Zhou, X. Deng, J. Cui, *Adv. Mater.* **2020**, *32*, 2000870.
[18] J. Fei, D. Han, J. Ge, X. Wang, S. W. Koh, S. Gao, Z. Sun, M. P. Wan, B. F. Ng, L. Cai, H. Li, *Adv. Funct. Mater.* **2022**, *32*, 2203582.
[19] P. Li, A. Wang, J. Fan, Q. Kang, P. Jiang, H. Bao, X. Huang, *Adv. Funct. Mater.* **2022**, *32*, 2109542.
[20] J. Mandal, M. Jia, A. Overvig, Y. Fu, E. Che, N. Yu, Y. Yang, *Joule* **2019**, *3*, 3088.
[21] X.-H. Li, C. Liu, S.-P. Feng, N. X. Fang, *Joule* **2019**, *3*, 290.
[22] Q. Liu, Z. Liu, C. Li, K. Xie, P. Zhu, B. Shao, J. Zhang, J. Yang, J. Zhang, Q. Wang, C. F. Guo, *Adv. Sci.* **2020**, *7*, 2000348.
[23] M. Retsch, M. Schmelzeisen, H.-J. Butt, E. L. Thomas, *Nano Lett.* **2011**, *11*, 1389.
[24] L. F. Rojas-Ochoa, S. Romer, F. Scheffold, P. Schurtenberger, *Phys. Rev. E* **2002**, *65*, 051403.
[25] Y. Ke, J. Chen, C. Lin, S. Wang, Y. Zhou, J. Yin, P. S. Lee, Y. Long, *Adv. Energy Mater.* **2019**, *9*, 1902066.
[26] S. Wang, Y. Zhou, T. Jiang, R. Yang, G. Tan, Y. Long, *Nano Energy* **2021**, *89*, 106440.
[27] S. Liu, Y. Li, Y. Wang, K. M. Yu, B. Huang, C. Y. Tso, *Adv. Sci.* **2022**, *9*, 2106090.
[28] S. Liu, Y. W. Du, C. Y. Tso, H. H. Lee, R. Cheng, S.-P. Feng, K. M. Yu, *Adv. Funct. Mater.* **2021**, *31*, 2010426.

[29] Z. Fang, L. Ding, L. Li, K. Shuai, B. Cao, Y. Zhong, Z. Meng, Z. Xia, *ACS Photonics* **2021**, *8*, 2781.
[30] Q. Zhang, Y. Jiang, L. Chen, W. Chen, J. Li, Y. Cai, C. Ma, W. Xu, Y. Lu, X. Jia, Z. Bao, *Adv. Funct. Mater.* **2021**, *31*, 2100686.
[31] Y. Zhou, Y. Cai, X. Hu, Y. Long, *J. Mater. Chem. A* **2014**, *2*, 13550.
[32] L. Wang, X. Jiao, D. Chen, T. Wang, *Adv. Sci.* **2021**, *9*, 2104121.
[33] X. Liang, S. Guo, M. Chen, C. Li, Q. Wang, C. Zou, C. Zhang, L. Zhang, S. Guo, H. Yang, *Mater. Horizons* **2017**, *4*, 878.
[34] J. Mandal, Y. Fu, A. C. Overvig, M. Jia, K. Sun, N. N. Shi, H. Zhou, X. Xiao, N. Yu, Y. Yang, *Science* **2018**, *362*, 315.
[35] H. Zhang, K. C. S. Ly, X. Liu, Z. Chen, M. Yan, Z. Wu, X. Wang, Y. Zheng, H. Zhou, T. Fan, *Proc. Natl. Acad. Sci. USA* **2020**, *117*, 14657.
[36] H.-N. Kim, D. Ge, E. Lee, S. Yang, *Adv. Mater.* **2018**, *30*, 1803847.
[37] D. Ge, E. Lee, L. Yang, Y. Cho, M. Li, D. S. Gianola, S. Yang, *Adv. Mater.* **2015**, *27*, 2489.
[38] Y. Li, X. Wu, J. Li, K. Wang, G. Zhang, *Appl. Catal. B* **2018**, *229*, 218.
[39] H. Torres-Pierna, D. Ruiz-Molina, C. Roscini, *Mater. Horizons.* **2020**, *7*, 2749.
[40] H. Zhong, Y. Li, P. Zhang, S. Gao, B. Liu, Y. Wang, T. Meng, Y. Zhou, H. Hou, C. Xue, Y. Zhao, Z. Wang, *ACS Nano* **2021**, *15*, 10076.